PROF. MOJTABA BAGHERZADEH (Orcid ID : 0000-0003-3009-3693)

Article type : Research Article

New Magnetically Recyclable Reduced Graphene Oxide rGO/MFe_2O_4 (M= Ca, Mg)/Ag_3PO_4 Nanocomposites With Remarkably Enhanced Visible-light Photocatalytic Activity and Stability

Mojtaba Bagherzadeh*, Reyhaneh Kaveh

Department of Chemistry, Sharif University of Technology, PO Box 11155-3516, Tehran, Iran

Corresponding author's email: bagherzadeh@sharif.edu (M. Bagherzadeh)

ABSTRACT

New magnetically separable $CaFe_2O_4/Ag_3PO_4$, $MgFe_2O_4/Ag_3PO_4$, rGO/$CaFe_2O_4/Ag_3PO_4$ and rGO/$MgFe_2O_4/Ag_3PO_4$ photocatalysts synthesized by the hydrothermal and ion-exchange deposition method. These four types of photocatalyst were used for degradation of Methylene blue (MB), Methyl orange (MO) and 4-chlorophenol (4-CP) in aqueous solution under visible-light illumination. The optimized photocatalyst, i.e. rGO/$CaFe_2O_4/Ag_3PO_4$ with a mass ratio of (1:3:9) composite not only shows the highest photocatalytic performance for the degradation of MB, MO and 4-CP under visible light irradiation among the other synthesized photocatalysts but also exhibits high reusability and stability for at least 5 cycles. It was found that the impressive separation of electron-hole pairs as well as presence of rGO sheets which act as a high speed charge transfer were responsible for increasing photocatalytic

This article has been accepted for publication and undergone full peer review but has not been through the copyediting, typesetting, pagination and proofreading process, which may lead to differences between this version and the Version of Record. Please cite this article as doi: 10.1111/php.12968

activity over the optimized photocatalyst under visible-light irradiation. A possible mechanism for the increased photocatalytic activity of the rGO/$CaFe_2O_4$/Ag_3PO_4 with a mass ratio of (1:3:9) composite was discussed in detail.

Keyword: Photocatalyst; Visible light; $CaFe_2O_4$; $MgFe_2O_4$; Ag_3PO_4; rGO

INTRODUCTION

In the ubiquitous scientific world, development of environmentally friendly catalysts is one of the more considerable issues. Semiconductor photocatalysis as a green technology to remove hazardous organic contaminates in water has attracted extensive attention, as it can use sunlight irradiation as the energy source [1–4].

In the past years, some new and efficient photocatalytic materials such as Ag-based photocatalysts have been developed in order to increase the visible-light activity. For instance, silver orthophosphate (Ag_3PO_4) is an efficient visible-light responsive photocatalyst, because of its perfect capabilities in the photodegradation of organic contaminates. Ag_3PO_4 has been considered a good semiconductor photocatalyst with high photooxidative capabilities for O_2 generation from water. Unfortunately, Ag_3PO_4 is light-sensitive and slightly soluble in aqueous media. Therefore, Ag_3PO_4 can be photo-corroded and decompose under light irradiation. Ag^+ is transformed into weakly active Ag during the photodegradation process, so photocatalytic activity of Ag_3PO_4 slowly decreases due to the photocorrsion by the photogenerated electrons and the practical application of Ag_3PO_4 is considerable limited [5–8].

In order to resolve this problem, recent studies have indicated that combining two or more semiconductors to prepare a composite structure protects the Ag_3PO_4 nanoparticles from dissolution in aqueous media. This strategy can enhance photocatalytic performance and stability of Ag_3PO_4 [9–13].

Some Ag_3PO_4-based hybrid composites have been prepared in order to improve photocatalytic performance and stability. For example, Ag/Ag_3PO_4 [2], TiO_2/Ag_3PO_4/graphene [14], Fe_3O_4-Ag_3PO_4/AgI [15], Ag_3PO_4/Bi_2MoO_6 [5], Ag_3PO_4/nitridized $Sr_2Nb_2O_7$ [16], Ag_3PO_4/Ag_2CO_3 [17], Ag_3PO_4/CeO_2 [18], Ag_3PO_4/rGO [19–21] have been synthesized and exhibited increased photocatalytic performance and stability than neat Ag_3PO_4. However, aforementioned composites cannot separate and recycle easily. To overcome this issue, magnetic composite photocatalysts have been developed. These kinds of composites can separate from aqueous media via an external magnet easily [8,22].

Spinel ferrites have considered worthy of attention due to their magnetic properties and the thermal and chemical stability of these particles. Spinel ferrites have been used for many applications such as preparing efficient and separable composite photocatalysts [23–27].

Calcium ferrite ($CaFe_2O_4$) and Magnesium ferrite ($MgFe_2O_4$) are suitable choices for fabrication of magnetic composite photocatalysts. $CaFe_2O_4$ and $MgFe_2O_4$ are visible-light responsive semiconductors with narrow bands gap of approximately 1.9eV and 2.18eV, respectively. Also, spinel ferrite-based catalysts can be easily separable because of their magnetic properties [28–34].

Up to now, coupling of Ag_3PO_4 with spinel ferrites is rare. Chen et al. fabricated a $ZnFe_2O_4/Ag_3PO_4$ photocatalyst which improved the photocatalytic activity compared with neat Ag_3PO_4 [35]. Zhao et al. synthesized $NiFe_2O_4/Ag_3PO_4$ photocatalysts that enhanced the photocatalytic performance towards the degradation of methylene blue [36].

In recent decades, reduced graphene oxide (rGO) has attracted tremendous attention in photocatalysis because of its unique properties such as large surface area, better electronic conductivity and good solution-dispersibility. In fact rGO is a good candidate for the preparation of different graphene-based composite photocatalysts [37–41].

The extensive presence of organic contaminates in waste water from industries or households is an serious environmental problem. These persistent organic chemicals can be found in groundwater [8,19].

For instance, chlorophenols such as 4-chlorophenol (4-CP) in aqueous solution are important micropollutants of the aquatic environment. Also, organic dyes (MB, MO, etc.) are an important source of water contamination. Many technologies have been employed over the years for water decontamination [42,43]. Among these various strategies, photocatalysis phenomenon has attracted attention because of the simplicity, high reproducibility and perfect performance.

The aim of this work is to prepare magnetically separable visible-light responsive photocatalysts, which are stable and easy to synthesize. $CaFe_2O_4/Ag_3PO_4$, $MgFe_2O_4/Ag_3PO_4$, $rGO/CaFe_2O_4/Ag_3PO_4$ and $rGO/MgFe_2O_4/Ag_3PO_4$ composites were successfully synthesized. The photocatalytic performance of these composites were evaluated by photo-degradation of 4-CP, MB, MO in water under visible-light irradiation. The synergistic effects of GO contents in $CaFe_2O_4/Ag_3PO_4$ and $MgFe_2O_4/Ag_3PO_4$ composites on the photocatalytic efficiency are investigated.

The present study opens promising perspectives for increasing visible-light-driven photocatalytic efficiency based on graphene oxide in order to destroy toxins.

MATERIALS AND METHODS

Reagents and apparatus. The materials including ferric nitrate ($Fe(NO_3)_3.9H_2O$), calcium nitrate ($Ca(NO_3)_2.6H_2O$), magnesium nitrate ($Mg(NO_3)_2.6H_2O$), silver nitrate ($AgNO_3$), sodium phosphate monobasic (NaH_2PO_4), sodium hydroxide (NaOH) , graphite powder, MB ($C_{16}H_{18}ClN_3S$), MO ($C_{14}H_{14}N_3NaO_3S$), 4-chlorophenol (4-CP), were extra pure and purchased from Merck company and used without further purification. Other chemicals and solvents such as ethylene glycol (EG), ethanol (C_2H_6O) were of analytical grade and used as received.

Fourier transform infrared (FTIR) spectra of the prepared samples were recorded on a Bruker Tensor 27 spectrometer using a KBr pellet for sample preparation at room temperature. The structure of samples were investigated via using X-ray diffraction (XRD) technique that were carried out on an Inel Equinox 3000 X-ray diffractometer using Cu Kα radiation. Raman measurements (wavelength 532 nm) were acquired by an Upright Raman microscope with DPSSVD: YAG type of laser excitation. The magnetization of the prepared samples was measured with vibrating sample magnetometer (VSM) (Lake Shore Model 7400, Japan) operating at room temperatures. Optical absorption spectra of the prepared samples were investigated by Ultraviolet−visible (UV−vis) diffuse-reflectance spectra (DRS) on an Avaspec-2048-TEC UV−vis−NIR spectrometer that Barium sulfate ($BaSO_4$) powder was the internal standard in the wavelength range of 200−800 nm. All of the binding energies were determined by this method. Photoluminescence (PL) spectroscopy was monitored using a CARY ECLIPSE fluorescence spectrometer. The morphology and particle distribution were performed by TESCAN MIRA II field emission scanning electron microscope. The electrochemical impedance spectra (EIS) were carried out by the Autolab potentiostat/galvanostat apparatus in a three electrodes cell. Pt wire as the counter electrode, Ag/AgCl (saturated KCl) as the reference electrode and 0.5 M Na_2SO_4 solution as the electrolyte were applied. EIS measurements were also gained at the open-circuit voltage and these measurements were taken in the frequency range from 0.1 Hz to 100 kHz with AC amplitude of 5 mV. In order to fabricate of working electrode, 30 mg as-prepared catalyst powder and 1 mL ethanol solution were sonicated and then the mixture was sprayed on a 1×1 cm^2 area of FTO (fluorine doped tin oxide) glass and allowed to dry at 400 °C for 1 h in furnace. The EIS measurements were carried out at room temperature (25 °C). A 500 W xenon lamp source equipped with AM 1.5G filter was used as the light source.

Synthesis of MFe_2O_4 (M= Ca, Mg)/Ag_3PO_4 photocatalysts. MFe_2O_4 (M= Ca, Mg)/Ag_3PO_4 composites were synthesized by an ion-exchange method. In the first step, MFe_2O_4 nanoparticles were prepared by simple hydrothermal method. The calcium nitrate $Ca(NO_3)_2.6H_2O$ and ferric nitrate $Fe(NO_3)_3.9H_2O$ with a molar ratio of (1:2) were added into 60 mL ethylene glycol (EG). After being sonicated for 10 min, the pH of the solution was adjusted to 10 using an appropriate NaOH solution. Then the resulting mixture was transferred into a 100 mL Teflon-lined autoclave and heated to 125 $^{\circ}$C for 24 h. After filtration and being washed several times with ethanol, the product was dried to obtain $CaFe_2O_4$ nanoparticles. The $MgFe_2O_4$ nanoparticles were synthesized by the same method by replacing the calcium nitrate with magnesium nitrate.

A procedure for preparing of $CaFe_2O_4$/Ag_3PO_4 composite with a mass ratio of (1:3) is as follows:

0.510 g (3 mmol) of $AgNO_3$ was solved in 20 mL distilled water and ammonia aqueous solution (1.0 M) was added gradually to the aforementioned solution in order to form a transparent solution. Then 0.17 g $CaFe_2O_4$ was added into the solution and resulting mixture was sonicated for 30 min. 10 mL aqueous solution of NaH_2PO_4 (0.1 M) was added with drop by drop to the above mixture while sonication, then prepared mixture was sonicated for another 30 min. The precipitates were filtered and being washed with distilled water and dried at 80 °C for 24 h (Scheme 1). The $MgFe_2O_4$/Ag_3PO_4 composite (1:3) were prepared via the same procedure by replacing synthesized $MgFe_2O_4$ nanoparticles with $CaFe_2O_4$ nanoparticles.

The Ag_3PO_4 nanoparticles was prepared by a similar method without adding $CaFe_2O_4$ or $MgFe_2O_4$ nanoparticles.

Synthesis of the rGO/ MFe_2O_4 (M= Ca, Mg)/ Ag_3PO_4 photocatalysts. Graphene oxide (GO) was synthesized from purified graphite powder based on Hummers method [39]. In order to synthesize rGO/ $CaFe_2O_4$ composite a hydrothermal method was used. First $Ca(NO_3)_2.6H_2O$ and $Fe(NO_3)_3.9H_2O$ with a molar ratio of (1:2) were dissolved into 60 mL EG and treated with sonicate for 10 min. Second, 0.056 g GO was dispersed into 10 mL EG. After being sonicated for 1 h, two solutions were mixed together and sonicated for another 1 h. Then suitable amount of NaOH solution was added to resulting solution until the pH reached 10. The mixture was transferred into a 100 mL sealed Teflon-lined autoclave for 24 h at 125 °C. The prepared precipitate was washed with ethanol and dried to obtain rGO/ $CaFe_2O_4$ nanoparticles. Some amount of oxygen- containing groups in GO reduced during the hydrothermal reaction process, so the products of rGO are in the prepared composite. The similar method by replacing the calcium nitrate with magnesium nitrate was applied in order to synthesize rGO/ $MgFe_2O_4$ nanopaticles.

For typical preparation of rGO/MFe_2O_4(M= Ca, Mg)/Ag_3PO_4 composites with a mass ratio of (1:3:9), 0.510 g $AgNO_3$ were dispersed into 20 mL distilled water and ammonia aqueous (1.0 M) was added dropwise into the solution of $AgNO_3$. Then 0.17 g rGO/ MFe_2O_4(M= Ca, Mg) was added into the mixture sonicated about 2 h in order to make Ag^+ combine with the surface of rGO/ MFe_2O_4(M= Ca, Mg). After that, 10 mL NaH_2PO_4 (0.1 M) was added into the above solution gradually. The prepared mixture was sonicated for another 30 min. Finally, the product was collected and washed with distilled water and dried at 80 °c for 2 h.

Photocatalytic activity measurement. The photodegradation performance of the synthesized samples were evaluated for MB, MO and 4-CP degradation in aqueous solution under visible light irradiation. A 250-W mercury lamp with a cut off filter (providing visible light $\geq$ 420 nm) as the light source was employed. Photocatalytic experiment was carried out in a 150 mL photoreactor at room temperature (25 °C ± 2 °C). In all of the measurements, distance between the lamp and the reactor was kept at 50 cm and its focused intensity on the reactor was calculated 85.272 $\mu W.cm^{-2}$. Fig. 1 shows the emission wavelength of the 250-W mercury lamp with the UV cut-off filter. For each experiment, a desired amount of prepared photocatalyst (0.5-3 g/L) was added to the MB, MO and 4-CP aqueous solutions with a favorite concentration of pollutant (15-35 mg/L) and illumination under continuous stirring. Prior to irradiation, the solution was stirred in the dark for 1 h to obtain an equilibrium between MB, MO and 4-CP aqueous solution and prepared photocatalysts. Then, the mixture was exposed to Mercury lamp illumination under continuous stirring. At a given time interval of irradiation, 5 mL of the reaction mixture was withdrawn and photocatalyst was magnetically separated. The concentration of the residual MB, MO and 4-CP in the reaction of solution were monitored by measuring the absorbance of solution at the wavelength 667, 469 and 280 nm respectively.

To study the reaction kinetic of photodegradation reaction of MB, MO and 4-CP under visible light illumination, the pseudo-first-order model called Langmuir-Hinshelwood (L-H) kinetic was used (Eq. (1)) [44].

$$r = -\frac{dC}{dt} = \frac{kKC}{1 + KC} \tag{1}$$

In which r, C, t, k and K are degradation rate (mg L^{-1} min^{-1}), organic pollutant concentration in aqueous solution after the various intervals of time (mg L^{-1}), irradiation time (min), reaction rate constant (min^{-1}) and adsorption coefficient of organic pollutant (L mg^{-1}), respectively. At low initial concentration of organic pollutant, the Eq. (1) is reduced to the Eq. (2):

$$r = -\frac{dC}{dt} = K_{app}\, C \tag{2}$$

Where K_{app} is gained for organic pollutant photodegradation from plotting the graph of $\ln(C_0/C_t)$ versus t.

The photocatalytic stability of the prepared photocatalysts was investigated by using repeated test for MB, MO and 4-CP degradation. After reaction in each test, the mixture was extracted to investigate the concentration of MB, MO and 4-CP, while the reacted prepared photocatalysts were collected via an external magnet and dried at 80 °C for the next run.

Also, the free radical trapping experiments were carried out. Tert-butyl alchol (t-BuOH) was chosen as the hydroxyl radical ($^{\bullet}OH$) scavenger, benzoquinone (BZQ) was chosen as the superoxide radical ($O_2^{\bullet-}$) scavenger, KI was chosen as the hole (h^+) scavenger.

RESULTS AND DISCUSSION

Characterizations

FT-IR spectroscopy. Fig. 2 displays FT-IR spectra of $CaFe_2O_4$, Ag_3PO_4, $CaFe_2O_4/Ag_3PO_4$ and rGO/$CaFe_2O_4/Ag_3PO_4$ nanoparticles. As shown in Fig. 2a, the FT-IR spectrum exhibits the characteristic peaks of the calcium ferrite skeleton. The small peak appeared at 3408 cm^{-1} indicated the stretching vibration of the O-H band. Presence of this small peak is attributed to adsorbed water at the surface of calcium ferrite nanoparticles. Also, the band at 2501 cm^{-1} is corresponding to the trace of atmospheric or adsorbed CO_2. The peak at 1433 cm^{-1} can be attributed to the C-H bending frequencies of the remaining trace of EG. The band at 881cm^{-1} correspond to Fe-O-H bending vibrations and the bands at 487 and 455 cm^{-1} attributed to the stretching vibration of the Ca-O and Fe-O (metal-oxygen bonds) [32,45].

Fig. 2b shows the FT-IR spectrum of Ag_3PO_4 nanoparticles. The band at 3176 cm^{-1} is attributed to the O-H stretching of water molecules. The sharp peak at 1388cm^{-1} is related to the antisymmetric stretching mode of the PO_4^{3-} group, whereas the symmetric vibration mode of PO_4^{3-} group is found at 763cm^{-1}. The asymmetric stretching vibration of P-O bonds is found at 1020 cm^{-1}. Also, the peak at 547cm^{-1} is attributed to the asymmetric bending mode of P-O bonds [46].

In spectrum of $CaFe_2O_4/Ag_3PO_4$ (1:3), the absorption peak at 422 and 462 cm^{-1} ascribed metal-oxygen bonds that become weak and the absorption peaks at 555, 759 and 1020 cm^{-1} can be assigned to the symmetric bending mode of P-O bonds, symmetric vibration mode of PO_4^{3-} group and asymmetric stretching vibration of P-O bonds, respectively (Fig. 2c). In spectrum of rGO/$CaFe_2O_4/Ag_3PO_4$ (1:3:9) composite (Fig. 2d), the peak at 1541 cm^{-1} appear due to the skeletal vibration of graphene [47].

Fig. S1a (see Supporting Information file) shows FT-IR spectra of $MgFe_2O_4$ nanoparticles. The absorption bands at 3454 and 1629 cm^{-1} are attributed to vibration of bonded O-H and H-O-H of adsorbed water hydroxyl ions. The band at 881 cm^{-1} is related to Fe-O-H vibrations in FeOOH. The peaks at 490, 492 and 457 cm^{-1} correspond to the vibrations of metal oxygen bonds such as Mg-O and Fe-O. The band at 1438 cm^{-1} may be related to C-H bending frequencies of remaining trace EG [45,48].

Fig. S1b exhibits the spectra of Ag_3PO_4 nanoparticles and Fig. S1c displays the FT-IR spectra of $MgFe_2O_4/Ag_3PO_4$ (1:3) composite. The peaks at 486 and 524 cm^{-1} are assigned to the vibrations of metal-oxygen bonds. The bands at 557 and 767cm^{-1} are attributed to the symmetric bending mode of P-O bonds and symmetric vibration mode of PO_4^{3-}, respectively. The peak at 1037 cm^{-1} is related to asymmetric stretching vibration of P-O bonds. As shown in Fig. S1d that is related to the sample of rGO/$MgFe_2O_4$/Ag_3PO_4 (1:3:9) the band at 1541 cm^{-1} correspond to the skeletal vibration of graphene.

XRD analysis. Fig. 3 shows X-ray diffraction pattern of prepared Ag_3PO_4, $CaFe_2O_4$, $CaFe_2O_4$/Ag_3PO_4 and rGO/$CaFe_2O_4$/Ag_3PO_4 nanoparticles. All diffraction peaks can be indexed to Ag_3PO_4 (JCPDS NO. 6-0505) or $CaFe_2O_4$ (JCPDS NO. 74-2136). The XRD pattern of $CaFe_2O_4$/Ag_3PO_4 (1:3) depicted in Fig. 3b indicates that the material obtained contains just $CaFe_2O_4$ and Ag_3PO_4. Also, at the XRD pattern of rGO/$CaFe_2O_4$/Ag_3PO_4 composite no typical peak of GO at $2\theta \sim 10$ was observed that is due to the presence of $CaFe_2O_4$ and Ag_3PO_4 nanoparticles between interlayers during the reduction process.

As shown in Fig. S2, the diffraction peaks of $MgFe_2O_4$ are in agreement with standard diffraction pattern of $MgFe_2O_4$ (JPDC NO. 36-0398). The XRD pattern of $MgFe_2O_4$/Ag_3PO_4 (1:3) indicated that this sample obtained contains $MgFe_2O_4$ and Ag_3PO_4 nanoparticles and no other impurities are observed. In Fig. S2b, no peak of GO was detected. This issue is related to the presence of $MgFe_2O_4$ and Ag_3PO_4 nanoparticles between interlayer of GO sheets [14,46,49,50].

FE-SEM images. Fig. 4a and Fig. S3a showed the FE-SEM micrograph of prepared $CaFe_2O_4$ and $MgFe_2O_4$ nanoparticles, respectively. The micrographs showed the formation of spherical $CaFe_2O_4$ and $MgFe_2O_4$ nanoparticles. $CaFe_2O_4$ nanoparticles have diameter distribution between 100-200 nm. The estimated particle size of $MgFe_2O_4$ nanoparticles were in the range of 50-70 nm. FE-SEM images of rGO/$CaFe_2O_4$ and rGO/$MgFe_2O_4$ composites were shown in Fig. 4b and Fig. S3b, respectively. In a comparision, in Fig 4b, S3b homogenous spherical particles of $CaFe_2O_4$ and $MgFe_2O_4$ were loaded on graphene's surface. Presence of graphene's sheets could be vividly limited the aggregation and size of synthesized spinel ferrites. It could be seen that prepared calcium ferrite had better interaction with graphene's sheets than magnesium ferrite.

Morphology of the prepared Ag_3PO_4 nanoparticles was observed in Fig. 4c. As can be seen from Fig. 4c, prepared Ag_3PO_4 particles have irregular particles morphology.

The FE-SEM images of $CaFe_2O_4/Ag_3PO_4$ and $MgFe_2O_4/Ag_3PO_4$ composites were shown in Fig. 4d and Fig. S3c, respectively. It can be seen that the $CaFe_2O_4$ and $MgFe_2O_4$ particles scattered on the surface of Ag_3PO_4 particles in aforementioned images.

Fig. 4e, f and Fig. S3d, S3e displayed the FE-SEM images of synthesized $rGO/CaFe_2O_4/Ag_3PO_4$ and $rGO/MgFe_2O_4/Ag_3PO_4$ composites, respectively. The images of the rGO/MFe_2O_4 (M=Ca, Mg)/Ag_3PO_4 with a mass ratio of (1:3:9) indicate that rGO sheets are embedded between the crystal particles. The calcium and magnesium ferrite nanoparticles are agglomerated around the Ag_3PO_4 crystal to form a composite structure.

Raman analysis. Fig. 5 compares the Raman spectra of both $CaFe_2O_4$ and $rGO/CaFe_2O_4$ nanoparticles. The $CaFe_2O_4$ Raman plot shows the typical peaks at 440, 566, 649 and 1246 cm^{-1}, respectively. The Raman plot of $rGO/CaFe_2O_4$ composites show the characteristics D and G peaks at 1359 cm^{-1} and 1571 cm^{-1} in addition to the peaks that were related to $CaFe_2O_4$ nanoparticles.

Fig. S4 exhibites the Raman plot of $MgFe_2O_4$ and $rGO/MgFe_2O_4$ nanoparticles. The peaks in the range of 100-1000 cm^{-1} were observed [43]. These peaks confirmed the pure $MgFe_2O_4$ nanoparticles. In Fig. S4b that is related to the $rGO/MgFe_2O_4$ composites in addition to the peaks corresponding to $MgFe_2O_4$, the characteristics D and G peaks at 1359 cm^{-1} and 1563 cm^{-1} appear which confirmed the dispersion of graphene oxide into reduced graphene oxide.

VSM Magnetic analysis. The magnetic response of pure $CaFe_2O_4$, $rGO/CaFe_2O_4/Ag_3PO_4$ and $MgFe_2O_4$ and $rGO/MFe_2O_4/Ag_3PO_4$ (1:3:9) nanoparticles has been investigated by VSM. (Fig. 6 and S5). It could be observed that presence of MFe_2O_4 (M= Ca, Mg) nanoparticles introduce the magnetic behavior in rGO/MFe_2O_4 (M= Ca, Mg)/Ag_3PO_4 composites. A drop in M_S values has been observed from 30.2 emu/gm and 26.9 emu/gm for $CaFe_2O_4$ and $MgFe_2O_4$ to 7 and 5 emu/gm for $rGO/CaFe_2O_4/Ag_3PO_4$ and $rGO/MgFe_2O_4/Ag_3PO_4$ nanoparticles, respectively. The lower values of the M_s can be related to the presence of Ag_3PO_4 particles and rGO sheets in the rGO/MFe_2O_4 (M= Ca, Mg)/Ag_3PO_4 composites. However the magnetic behavior of rGO/MFe_2O_4 (M= Ca, Mg)/Ag_3PO_4 composites allow their easy separation from suspended system by an external magnet [51].

UV-vis analysis. Fig. 7a, b and Fig. S6a exhibits the UV-vis diffuse reflectance spectroscopy of the $CaFe_2O_4$, Ag_3PO_4 and $MgFe_2O_4$ nanoparticles, respectively. The band gap energy (E_g) of these three samples were calculated by the following equation:

$$\alpha h\upsilon = A\ (h\upsilon - E_g)^{1/2} \qquad (3)$$

Where α is absorption coefficient and h is plank constant. Furthermore, υ and A are light frequency and a constant, respectively. E_g can be obtain from a region in the plot of $(\alpha h\upsilon)^2$ versus photon energy (hυ) [37].

The band gap energy of the pure $CaFe_2O_4$, $MgFe_2O_4$ and Ag_3PO_4 nanoparticles are about 1.52, 1.68 and 1.94 eV respectively. The E_g of these three samples are low compared to standard value, which can attribute to the different conditions of synthetic hydrothermal method. Diffuse reflectance spectroscopy of $CaFe_2O_4/Ag_3PO_4$ (1:3) and $MgFe_2O_4/Ag_3PO_4$ (1:3) composites are illustrated in Fig.7 and Fig. S6b, respectively. The value of E_g for $CaFe_2O_4/Ag_3PO_4$ composite was calculated 1.31 eV and this value for $MgFe_2O_4/Ag_3PO_4$ composite was 1.35 eV. So, these two composites have higher visible light absorption capability. Introduce of rGO sheets decreases band gap energy of $CaFe_2O_4/Ag_3PO_4$ and $MgFe_2O_4/Ag_3PO_4$ composites. The E_g for rGO/$CaFe_2O_4/Ag_3PO_4$ and rGO/$MgFe_2O_4/Ag_3PO_4$ composites obtained 1.17 and 1.20 eV, respectively (Fig. 7d and Fig. S6c). Consequently, rGO/$CaFe_2O_4/Ag_3PO_4$ composite has lower band gap energy compare to other samples.

PL results. The Photoluminescence (PL) analysis has been widely performed to study the migration, transfer and recombination processes of photo-induced electron-hole pairs in the prepared samples. In fact, the lower the PL signal means that the higher separation efficiency of photo-induced electron-hole pairs, implying that more photo-induced electrons and holes can be available for redox processes. Fig. S7 displays room temperature PL spectra of the pure Ag_3PO_4 nanoparticles, as well as rGO/MFe_2O_4 (M= Ca, Mg)/Ag_3PO_4 (1:3:9) composites upon the excitation wavelength at 420 nm. The main emission peak of Ag_3PO_4 was vividly decreased, owing to this fact that the recombination of photo-induced electron-hole pairs is efficiency prevented because of the presence of MFe_2O_4 nanoparticles and rGO sheets. As shown in Fig. S7 the weak pL intensity of rGO/MFe_2O_4 (M= Ca, Mg)/Ag_3PO_4 (1:3:9) composites, implying that the cooperative effects between MFe_2O_4/Ag_3PO_4 nanoparticles and rGO sheets contributed to enhancing the charge separation efficiency and decreasing the recombination of photogenerated electron-hole pairs effectively [52].

Electrochemical impedance measurement (EIS). EIS analysis was employed to obtain further insight into the charge transfer mechanisms. Fig. 8 exhibits the Nyquist plots of the synthesized Ag_3PO_4 and of rGO/MFe_2O_4 (M= Ca, Mg)/Ag_3PO_4 (1:3:9) composites at the open-circuit voltage. The semicircle diameter of EIS is equal to total charge transfer resistance (R_{ct}) in the prepared samples. As shown in Fig. 8 rGO/MFe_2O_4 (M= Ca, Mg)/Ag_3PO_4 (1:3:9) composites have smaller R_{ct} than pure Ag_3PO_4 nanoparticles, providing evidence that the rGO/MFe_2O_4 (M= Ca, Mg)/Ag_3PO_4 (1:3:9) composites have the low charge transfer resistance and high efficient separation of photoinduced electron-hole [53].

Photocatalytic performance for MB, MO and 4-CP degradation

Evaluation of the photocatalytic activity. To evaluate the photocatalytic performance of the synthesized samples, MB and MO photodegradation as well as 4-CP photodegradation were carried out under visible irradiation. MB, MO and 4-CP are representative organic contaminations. The control studies were also conducted without photocatalyst or light. The photocatalytic degradation was calculated as follow:

$$\% \text{ Degradation} = [(C_0-C_t)/C_0]*100 \quad (4)$$

Where C_0 and C_t are concentration of organic contaminations before irradiation and after irradiation, respectively.

First, the degradation efficiency for MB removal in the presence of prepared samples under visible light illumination were investigated.

The amount of MB adsorbed onto $CaFe_2O_4$, $CaFe_2O_4$/Ag_3PO_4 with a mass ratio of (1:3), rGO/$CaFe_2O_4$/Ag_3PO_4 (1:3:9) and $MgFe_2O_4$, $MgFe_2O_4$/Ag_3PO_4 (1:3), rGO/$MgFe_2O_4$/Ag_3PO_4 (1:3:9) was approximately evaluated to be ~ 4%, 9%, 12% and 5%, 8%, 9% of the initial amount of MB, respectively. As a result, the MB degradation without light irradiation could be neglected. As shown, the absence of any photocatalyst also concluded in no degradation, showing the removal of MB occurred through photocatalysis. Under aforementioned conditions, no electron-hole pairs can be formed and therefore photocatalytic behavior of synthesized samples is not induced. It is clear that the photocatalytic performances relate to the formation, transfer and separation of photogenerated electron-hole pairs [53-55]. As shown in Fig. 9, pure $CaFe_2O_4$ degraded only 21% of MB after 45 min while,

$CaFe_2O_4/Ag_3PO_4$ with a mass ratio of (1:3) showed 95% removal after 45 min that is related to the combine $CaFe_2O_4$ and Ag_3PO_4 nanoparticles together. The CB potential of $CaFe_2O_4$ is more negative than that Ag_3PO_4, so the photogenerated electrons in $CaFe_2O_4$ could migrate to the surface of Ag_3PO_4 and simultaneously, the photogenerated holes in the VB of Ag_3PO_4 could migrate to $CaFe_2O_4$. Aforementioned process could improve the separation of photogenerated electron-hole pairs. Based on the degradation efficiency results, the $rGO/CaFe_2O_4/Ag_3PO_4$ (1:3:9) degraded 92% of MB within 27 min. The high photocatalytic performance of $rGO/CaFe_2O_4/Ag_3PO_4$ could be attributed to the efficient separation of photogenerated electron-hole pairs. The rGO is a perfect electron acceptor and electron transporter which increases the charge separation efficiency that avoid recombining the photogenerated electron-hole pairs. Also, rGO keeps nanoparticles dispersed hence retards agglomeration. Consequently, photocatalytic activity could improve. Pure $MgFe_2O_4$ and $MgFe_2O_4/Ag_3PO_4$ with a mass ratio of (1:3) degraded 18% and 89% of MB after 45 min. The $rGO/MgFe_2O_4/Ag_3PO_4$ (1:3:9) composite showed 85% removal after 27 min (Fig. S8). Photocatalytic degradation efficiency of MO in the presence of pure $CaFe_2O_4$, $CaFe_2O_4/Ag_3PO_4$ (1:3), $rGO/CaFe_2O_4/Ag_3PO_4$ (1:3:9) and pure $MgFe_2O_4$, $MgFe_2O_4/Ag_3PO_4$ (1:3), $rGO/MgFe_2O_4/Ag_3PO_4$ (1:3:9) under visible light irradiation are presented in Fig. 10 and Fig. S9, respectively. The amount of MO adsorbed onto $CaFe_2O_4$, $CaFe_2O_4/Ag_3PO_4$ (1:3), $rGO/CaFe_2O_4/Ag_3PO_4$ (1:3:9) and $MgFe_2O_4$, $MgFe_2O_4/Ag_3PO_4$ (1:3), $rGO/MgFe_2O_4/Ag_3PO_4$ (1:3:9) was evaluated to be ~ 6%, 5%, 9% and 5%, 6%, 8% of the initial amount of MO, respectively. Consequently, the MO degradation without light could be neglected.

It is cleared that with decreasing band gap energies of the synthesized composites, photoactivity of prepared samples increase. In addition to MB and MO, 4-CP was selected as another model organic pollutant in order to further investigated the photocatalytic activity of the $rGO/CaFe_2O_4/Ag_3PO_4$ (1:3:9) and $rGO/MgFe_2O_4/Ag_3PO_4$ (1:3:9) that showed better photocatalytic performance in dye degradation compare to $CaFe_2O_4/Ag_3PO_4$ (1:3) and $MgFe_2O_4/Ag_3PO_4$ (1:3) composites. As shown in Fig. 11, after 160 min of irradiation, no degradation of 4-CP observed without catalysts. The photocatalytic degradation of 4-CP in the presence of $rGO/CaFe_2O_4/Ag_3PO_4$ (1:3:9) and of $rGO/MgFe_2O_4/Ag_3PO_4$ (1:3:9) under visible light was 90% and 86% in about 160 min, respectively.

The photocatalytic kinetics of the synthesized photoctalysts were also studied. K_{app} is gained for photodegradation of MB, MO and 4-CP from plotting the graph of ln (C_0/C_t) versus t as shown in Fig. 12, S10 and S11, respectively. Based on the k_{app} values, one can compare the photocatalytic performance of the various catalysts. The obtained results displayed that the kinetic simulation curves are close to linear curves. All of the correlation coefficients (R^2) were higher than 0.9. Consequently, the pseudo first order kinetics model fit the experimental data well [56,57]. As a result, the photocatalytic degradation of MB, MO and 4-CP using synthesized photoctalysts were fitted using the pseudo-first-order L-H model. As seen in Fig. 13, S12 and S13, the degradation rate of MB, MO and 4-CP in the presence of rGO/$CaFe_2O_4$/Ag_3PO_4 (1:3:9) under visible light illumination was higher than of others.

Effect of concentration of catalyst on pollutants photodegradation. The effect of rGO/$CaFe_2O_4$/Ag_3PO_4 (1:3:9) photocatalyst concentration on the photodegradation rate of MB, MO and 4-CP were investigated in the range of 0.5 g/L to 3 g/L at constant pollutants concentration (25 mg/L) and the obtained results are illustrated in Fig. 14, S14 and S15, respectively. As shown, the photodegradation efficiency of MB, MO and 4-CP enhances from 0.5 to 2 g/L. At low photocatalyst concentration, the adsorbed light controlled the activity of photocatalyst. It could be attributed to the limited photocatalyst surface area. On the other hand, further raising the photocatalyst concentration from 2 to 3 g/L has a negative effect on the photodegradation efficiency. This issue may cause enhanced scattering and turbidity effects, resulting in decreased visible light penetration on the synthesized photocatalyst surface and into the solution. The results showed that the optimum photocatalyst concentration for pollutants degradation was 2 g/L.

Effect of initial pollutants concentration on photodegradation. Fig. 14, S16 and S17 illustrate the interaction effect of initial MB, MO and 4-CP concentration on the degradation rate of pollutants by changing the initial concentration of pollutants from 15 to 35 mg/L with constant photocatalyst concentration (2 g/L) under visible light irradiation, respectively. As the pollutants concentration increases, the amount of pollutants adsorbed on the active surface area of photocatalyst enhances. As a result, the formation of $^{\bullet}OH$ radicals will be enhanced. The obtained results showed that the photodegradation efficiency of pollutants decrease with increase in initial MB, MO and 4-CP concentration ranging from 25 to 35 mg/L. The increase in initial pollutants concentration decrease the visible light penetration to the surface of photocatalyst. Furthermore, the limited active site onto the photocatalyst may be another reason for the decreased photodegradation efficiency.

Effect of reactive species on photodegradation of pollutants. In order to further insight into the photodegradation pathway of organic pollutants, the free radical trapping experiments to investigate the role of reactive species in the photocatalytic system of rGO/CaFe2O4/Ag3PO4 (1:3:9) were carried out. The degradation efficiency of MB, MO and 4-CP under various scavengers (t-BuOH as the hydroxyl radical ($^{\bullet}$OH) scavenger, BZQ as the superoxide radical ($O_2^{\bullet -}$) scavenger and KI as the hole (h^+) scavenger) are shown in Fig.15, S18 and S19, respectively [58].

As observed in Fig. 15, MB strongly degraded after 27 min photocatalytic treatment without scavengers, while the addition of 1 mM t-BuOH scavenger caused fast deactivation of the rGO/CaFe2O4/Ag3PO4 (1:3:9) photocatalyst, and the degradation efficiency of MB decreased from 92% to 41% in 27 min. So, this result indicates that all $^{\bullet}$OH play main role in this process. The introduction of 1 mM BZQ into the system also restrained the photocatalytic activity of the photocatalyst toward MB after 27 min reaction, demonstrating that $O_2^{\bullet -}$ play an important role in photodegradation. When the 1mM KI was introduced into the system, the degradation rate was slightly reduced indicating that h^+ has little effect on the MB degradation. The same observations for MO and 4-CP degradation exhibit $^{\bullet}$OH participation which was formed by oxidative and reductive reactions as well as $O_2^{\bullet -}$ is the great contributor for pollutants degradation.

Photocatalytic stability. Stability of the rGO/$CaFe_2O_4$/Ag_3PO_4 with a mass ratio of (1:3:9) that had higher photocatalytic activity as compared to other synthesized photocatalysts is another essential factor for evaluating its performance. Therefore, rGO/$CaFe_2O_4$/Ag_3PO_4 was recycled for five times under the same conditions. The degradation of MB, MO and 4-CP during each run is exhibited in Fig. 16a, b and c, respectively. The photocatalytic data showed that photocatalytic activity of rGO/$CaFe_2O_4$/Ag_3PO_4 (1:3:9) for organic contaminations degradation changes little and even, 84%, 80% and 74% of MB, MO and 4-CP is degraded after recycling for five times, respectively. In fact, after contact between Ag_3PO_4 and $CaFe_2O_4$ particles, a p-n junction is generated, the charge carriers transfer from $CaFe_2O_4$ to Ag_3PO_4. Consequently, the rGO/$CaFe_2O_4$/Ag_3PO_4 displays high stability because it does not suffer from photocorrosion during the degradation contaminates. In addition, the rGO sheets not only enhance the charge separation efficiency but also keep nanoparticles dispersed hence retards agglomeration so the rGO/$CaFe_2O_4$/Ag_3PO_4 photocatalyst shows high stability. The used photocatalysts separated by an external magnetic field was washed with distilled water for two times and dried at 80 °C for 1 h.

Possible photocatalytic mechanism in rGO/MFe_2O_4 *(M= Ca, Mg)/*Ag_3PO_4 *system.* In order to elucidate photocatalytic degradation mechanism of organic pollutants over synthesized photocatalysts, the reactive species including $^{\bullet}OH$, $O_2^{-\bullet}$ and h^+ involved in the photodegradation process were investigated. The photodegradation pathway of MB, MO and 4-CP over the prepared photocatalysts could be inferred, which is illustrated in Scheme 2 [59–62]. To clarify the separation of photo-induced e^-/h^+ pairs over the synthesized photocatalysts, it is essential to estimate the conduction band (CB) and valence band (VB) potentials of the samples. These energy levels were calculated using the following equations:

$$E_{CB} = \chi - E^e - 0.5\ E_g \tag{5}$$

$$E_{VB} = E_{CB} - E_g \tag{6}$$

Where E_{VB}, E_{CB} and E^e are the VB, CB potentials and the energy of free electrons vs. hydrogen (4.5 eV), respectively. Also, χ is electronegativity of the semiconductor and it was estimated via Eq. (13):

$$\chi = [\chi\ (A)^a\ \chi\ (B)^b\ \chi\ (C)^c]^{1/a+\ b+\ c} \tag{7}$$

In above equation a, b, and c are the number of atoms in the compounds [63]. The values of E_g and χ for Ag_3PO_4 are 1.94 and 5.98 eV, respectively. So, the E_{CB} and E_{VB} of Ag_3PO_4 were estimated to be 0.51 and 2.45 eV versus normal hydrogen electrode (NHE). Moreover, the estimated values of E_g and χ for $CaFe_2O_4$ are 1.52 and 5.54 eV, respectively. As a result, E_{CB} and E_{VB} for $CaFe_2O_4$ are 0.28 and 1.8 eV. E_g and χ for $MgFe_2O_4$ are 1.64 and 5.67 eV, respectively. Therefore, the E_{CB} and E_{VB} of $MgFe_2O_4$ were estimated to be 0.35 and 1.99 eV. For CaF_2O_4 and $MgFe_2O_4$ particles that are p-type semiconductors, the Fermi levels are close to VB levels and for Ag_3PO_4 particles which are n-type semiconductor, the Fermi level is close to CB level.

Before contact between Ag_3PO_4 and MFe_2O_4 particles, the CB edge and Fermi level of Ag_3PO_4 are lower than those of MFe_2O_4. After contact when a p-n junction is generated, the charge carriers transfer from MFe_2O_4 to Ag_3PO_4. Consequently, an external electric field at the heterojunction interface is generated [64]. The Fermi energy levels of n-Ag_3PO_4 and p-MFe_2O_4 are aligned under equilibrium conditions. In fact, the photogenerated electrons in

MFe_2O_4 could migrate to Ag_3PO_4 and simultaneously, the photogenerated holes in the VB of Ag_3PO_4 could migrate to MFe_2O_4. Aforementioned process could improve the separation of photogenerated electron-hole pairs. Consequently, the photogenerated electrons in CB of Ag_3PO_4 react with surface adsorbed O_2 to form $O_2^{\bullet -}$, which then reacts with H^+ to form $^{\bullet}OOH$, followed by rapid decomposition to $^{\bullet}OH$ radicals. In addition, the photogenerated holes in VB of MFe_2O_4 could oxidize H_2O and OH^- to form $^{\bullet}OH$ radicals, that are involved in the photodegradation reaction of organic pollutants. In fact, the process of generating $^{\bullet}OH$ can occur by two pathways.

$rGO/MFe_2O_4/Ag_3PO_4$ shows significant advance in photodegradation of organic pollutants compared to MFe_2O_4/Ag_3PO_4. The rGO sheets are perfect speed charge transfer ability that enhances the charge separation efficiency which prevent recombination of the photogenerated electrons and holes. The photogenerated electrons in MFe_2O_4 migrate to the rGO sheets due to marvelous electron conductivity and graphene sheets are good electron acceptors. So, the electrons are quickly migrate to the graphene sheets. Then, the electrons transferred to the surface of Ag_3PO_4 (Fig. 17 and S20). As a result, the electron-hole recombination of the $rGO/MFe_2O_4/Ag_3PO_4$ is inhibited. In addition, rGO sheets can delay aggregation of nanoparticles. So, the presence of rGO sheets in the composites can promote the separation of electron-hole pairs that this issue has a main role in the increase quantity of active holes for organic contaminations degradation also, the probability of combination of photogenerated electrons and Ag_3PO_4 decreases, that offers better recyclability and stability of the prepared composites.

CONCLUSIONS

In summary, we have successfully indicated four efficient and magnetically separable photocatalysts $CaFe_2O_4/Ag_3PO_4$, $MgFe_2O_4/Ag_3PO_4$, $rGO/CaFe_2O_4/Ag_3PO_4$ and $rGO/MgFe_2O_4/Ag_3PO_4$ for MB, MO and 4-CP degradation. It was shown that $rGO/CaFe_2O_4/Ag_3PO_4$ with a mass ratio of (1:3:9) nanocomposite exhibits the wonderful visible light photocatalytic activity compared with other synthesized nanocomposites, that arises from synergistic effect between the prepared nanocomposites and rGO sheets.

On the basis of this study, the $rGO/CaFe_2O_4/Ag_3PO_4$ nanocomposite photocatalytic system is an effective and magnetically recoverable visible light driven photocatalyst for degradation of MB, MO and 4-CP as representative of organic contaminations.

Acknowledgement

M.B. acknowledges the Research Council of Sharif University of Technology for the research funding of this project.

SUPPORTING INFORMATION

Additional Supporting Information is available in the online version of this article:

Fig. S1. FT-IR spectra of (a) $MgFe_2O_4$, (b) Ag_3PO_4, (c) $MgFe_2O_4/Ag_3PO_4$(1:3), (d) rGO/$MgFe_2O_4/Ag_3PO_4$(1:3:9).

Fig. S2. XRD patterns of (a) $MgFe_2O_4/Ag_3PO_4$; the iconograph in (a) is the XRD pattern of $MgFe_2O_4$ and (b) rGO/$MgFe_2O_4/Ag_3PO_4$.

Fig. S3. FESEM image of (a) neat $MgFe_2O_4$, (b) rGO/$MgFe_2O_4$, (c) $MgFe_2O_4/Ag_3PO_4$ (1:3), (d, e) rGO/$MgFe_2O_4/Ag_3PO_4$ (1:3:9).

Fig. S4. Raman spectra of (a) $MgFe_2O_4$ nanoparticles and (b) rGO/$MgFe_2O_4$ nanocomposites.

Fig. S5. Magnetization curve of $MgFe_2O_4$, rGO/$MgFe_2O_4/Ag_3PO_4$ (1:3:9).

Fig. S6. The UV–Vis DRS and the band gap for (a) $MgFe_2O_4$, (b) $MgFe_2O_4/Ag_3PO_4$(1:3), (c) rGO/$MgFe_2O_4/Ag_3PO_4$(1:3:9).

Fig. S7. Photoluminescence spectra with an excitation of a diode laser (wavelength 420 nm) of Ag_3PO_4, rGO/$CaFe_2O_4/Ag_3PO_4$ (1:3:9), rGO/$MgFe_2O_4/Ag_3PO_4$ (1:3:9).

Fig. S8. The degradation efficiency for MB (25 mg/L) removal in the process of the $MgFe_2O_4$, $MgFe_2O_4/Ag_3PO_4$ and rGO/$MgFe_2O_4/Ag_3PO_4$ nanocomposites under visible light irradiation ([catalyst]= 2 g/L).

Fig. S9. The degradation efficiency for MO (25 mg/L) removal in the process of the $MgFe_2O_4$, $MgFe_2O_4/Ag_3PO_4$ and rGO/$MgFe_2O_4/Ag_3PO_4$ nanocomposites under visible light irradiation ([catalyst]= 2 g/L).

Fig. S10. Linear-log plot for the photocatalytic degradation of MO in the presence of prepared samples under visible light irradiation.

Fig. S11. Linear-log plot for the photocatalytic degradation of 4-CP in the presence of rGO/$CaFe_2O_4/Ag_3PO_4$ and rGO/$MgFe_2O_4/Ag_3PO_4$ nanocomposites under visible light irradiation.

Fig. S12. The degradation rate constant of the fabricated catalysts for the photocatalytic degradation of MO under visible light irradiation.

Fig. S13. The degradation rate constant of the fabricated catalysts for the photocatalytic degradation of 4-CP under visible light irradiation.

Fig. S14. The degradation efficiency for MO (25 mg/L) removal using different amount of rGO/$CaFe_2O_4$/Ag_3PO_4 (1:3:9) under visible light irradiation.

Fig. S15. The degradation efficiency for 4-CP (25 mg/L) removal using different amount of rGO/$CaFe_2O_4$/Ag_3PO_4 (1:3:9) under visible light irradiation.

Fig. S16. The degradation efficiency for MO removal using different concentration of initial dye in the presence of rGO/$CaFe_2O_4$/Ag_3PO_4 (1:3:9) under visible light irradiation ([catalyst]= 2g/L).

Fig. S17. The degradation efficiency for 4-CP removal using different concentration of initial pollutant in the presence of rGO/$CaFe_2O_4$/Ag_3PO_4 (1:3:9) under visible light irradiation ([catalyst]= 2g/L).

Fig. S18. Effect of different scavengers on degradation of MO by rGO/$CaFe_2O_4$/Ag_3PO_4 under the optimized conditions.

Fig. S19. Effect of different scavengers on degradation of 4-CP by rGO/$CaFe_2O_4$/Ag_3PO_4 under the optimized conditions.

Fig. S20. Schematic illustration of the proposed reaction mechanism for the photocatalytic degradation of the dyes in the presence of rGO/$MgFe_2O_4$(M=Ca, Mg)/Ag_3PO_4 nanocomposite.

References

1. J. Fenoll, N. Vela, I. Garrido, G. Navarro, G. Lucas, S. Navarro (2015) Reclamation of Water Polluted with Flubendiamide Residues by Photocatalytic Treatment with Semiconductor Oxides. J. Photochem. Photobiol. 91, 1088–1094.

2. X. Huang, J. Ding, Q. Zhong (2015) Catalytic decomposition of H_2O_2 over Fe-based catalysts for simultaneous removal of NO_X and SO_2. Appl. Surf. Sci. 326, 66–72.

3. C. Guo, L. Song, Sh. Zhang (2018) Synthesis of $Pb_9(PO_4)_6$/Ag_3PO_4 Composite Photocatalysts With Enhanced Visible Light Photocatalytic Activity. J. Photochem. Photobiol. 94, 228-236.

4. L. Zhang, R. Zheng, S. Li, B. Liu, D. Wang, L. Wang, T. Xie (2014) Enhanced Photocatalytic H_2 Generation on Cadmium Sulfide Nanorods with Cobalt Hydroxide

as Cocatalyst and Insights into Their Photogenerated Charge Transfer Properties. Appl. Mater. Interfaces. 6, 13406−13412.

5. Yang-S. Xu, Wei-D. Zhang (2013) Monodispersed Ag_3PO_4 nanocrystals loaded on the surface of spherical Bi2MoO6 with enhanced photocatalytic performance. Dalton Trans. 42, 1094–101.

6. Y. Bi, Sh. Ouyang, N. Umezawa, J. Cao, J. Ye (2011) Facet effect of single-crystalline Ag_3PO_4 sub-microcrystals on photocatalytic properties. J. Am. Chem. Soc. 133, 6490–6492.

7. X. Zhao, L. Song, Sh. Zhang (2018) Synthesis of $AgCl/Ag_3PO_4$ Composite Photocatalysts and Study on Photodegradation Activity Based on a Continuous Reactor. J. Photochem. Photobiol. https://doi.org/10.1111/php.12875.

8. X. Chen, Y. Dai, J. Guo, T. Liu, X. Wang (2016) Novel Magnetically Separable Reduced Graphene Oxide (RGO)/$ZnFe_2O_4/Ag_3PO_4$ Nanocomposites for Enhanced Photocatalytic Performance toward 2,4-Dichlorophenol under Visible Light. Ind. Eng. Chem. Res. 55, 568–578.

9. X. Yang, H. Cui, Y. Li, J. Qin, R. H. Zhang, H. Tang (2013) Fabrication of Ag_3PO_4-graphene composites with highly efficient and stable visible light photocatalytic performance. Acs Catal. 3, 363–369.

10. B. Chai, J. Li, Q. Xu (2014) Reduced graphene oxide grafted Ag_3PO_4 composites with efficient photocatalytic activity under visible-light irradiation. Ind. Eng. Chem. Res. 53, 8744–8752.

11. Z. Yi, J. Ye, N. Kikugawa, T. Kako, S. Ouyang (2010) An orthophosphate semiconductor with photooxidation properties under visible-light irradiation. Nat. Mater. 9, 559–564.

12. Jing-W. Xu, Zhi-D. Gao, K. Han, Y. Liu, Yan-Y. Song (2014) Synthesis of magnetically separable $Ag_3PO_4/TiO_2/Fe_3O_4$ heterostructure with enhanced photocatalytic performance under visible light for photoinactivation of bacteria. ACS Appl. Mater. Interfaces. 6, 15122–15131.

13. W-S. Wang, H. Du, R-X. Wang, T. Wen, A-W. Xu (2013) Heterostructured Ag_3PO_4 /AgBr/Ag plasmonic photocatalyst with enhanced photocatalytic activity and stability

under visible light. Nanoscale. 5, 3315–3321.

14. X. Yang, J. Qin, Y. Jiang, R. Li, Y. Li, H. Tang (2014) Bifunctional TiO_2/Ag_3PO_4/graphene composites with superior visible light photocatalytic performance and synergistic inactivation of bacteria. RSC Adv. 4, 18627–18636.

15. A.M. Idris (2014) An In-Situ Anion Exchange Method Synthesized of Ag_3PO_4 Functionalized with Fe_3O_4 and AgI for Photocatalytic Degradation of Methyl Orange under Visible Light Irradiation. Int. J. Mater. Sci. Appl. 3, 303–308.

16. J. Guo, H. Zhou, S. Ouyang, T. Kako, J. Ye (2014) An Ag_3PO_4/nitridized $Sr_2Nb_2O_7$ composite photocatalyst with adjustable band structures for efficient elimination of gaseous organic pollutants under visible light irradiation. Nanoscale. 6, 7303–7311.

17. L. Ma, I. Jia, X. Guo, L. Xiang (2014) Current Status and perspective of rare earth catalytic materials and catalysis. Chinese J. Catal. 35, 108–119.

18. R. Shao, X. Zeng, Zh. Cao, H. Dong, L. Wang, F. Wang, J. Liu, Zh. Li, Q. Liang (2015) A novel Ag_3PO_4/Nb_2O_5 fiber composite with enhanced photocatalytic performance and stability. RSC Adv. 19, 673–679.

19. G. Chen, M. Sun, Q. Wei, Y. Zhang, B. Zhu, B. Du (2013) Ag_3PO_4/graphene-oxide composite with remarkably enhanced visible-light-driven photocatalytic activity toward dyes in water. J. Hazard. Mater. 244, 86–93.

20. B. Chai, J. Li, Q. Xu (2014) Reduced Graphene Oxide Grafted Ag_3PO_4 Composites with Efficient Photocatalytic Activity under Visible-Light Irradiation. Ind. Eng. Chem. Res. 53, 8744–8752.

21. Q. Xiang, D. Lang, T. Shen, F. Liu (2015) Graphene-modified nanosized Ag_3PO_4 photocatalysts for enhanced visible-light photocatalytic activity and stability. Appl. Catal. B, Environ. 162, 196–203.

22. J. Zhao (2017) Environmental Energy-efficient fabrication of a novel multivalence Mn_3O_4 -MnO_2 heterojunction for dye degradation under visible light irradiation. Applied Catal. B, Environ. 202, 509–517.

23. E. Casbeer, V. K. Sharma, X. Z. Li (2012) Synthesis and photocatalytic activity of ferrites under visible light: A review. Sep. Purif. Technol. 87, 1–14.

24. D. Guin, B. Baruwati, S.V. Manorama (2005) A simple chemical synthesis of nanocrystalline AFe_2O_4 (A= Fe, Ni, Zn): an efficient catalyst for selective oxidation of styrene. J. Mol. Catal. A Chem. 242, 26–31.

25. Zh. Li, X. Lai, H. Wang, D. Mao, Ch. Xing, D. Wang (2009) General synthesis of homogeneous hollow core-shell ferrite microspheres. J. Phys. Chem. C. Nanomater. Interfaces. 113, 2792–2797.

26. M. Aamir, Muhammad N. Ashiq, Gh. Yasmeen, B. Ahmad, Muhammad F. Ehsan, T. He (2015) Synthesis and characterization of polyaniline/ZrCo-substituted nickel ferrite ($NiFe_{1.2}Zr_{0.4}Co_{0.4}O_4$) nanocomposites: their application for the photodegradation of methylene blue. Desalin water treat. 57, 1–10.

27. H. Liu, H. Hao, J. Xing, J. Dong, Z. Zhang, Z. Zheng, K. Zhao (2016) Enhanced photocatalytic capability of zinc ferrite nanotube arrays decorated with gold nanoparticles for visible light-driven photodegradation of rhodamine B. J. Mater Sci. 51, 5872–5879.

28. William L. IV, J. Drwiega, David W. Mazyck, Seung W. Lee, W. Sigmund, Chang Y. Wu, P. Chadik (2005) Magnetically agitated photocatalytic reactor for photocatalytic oxidation of aqueous phase organic pollutants. Environ. Sci. Technol. 39, 8052–8056.

29. R. Dom, R. Subasri, K. Radha, P.H. Borse (2011) Synthesis of solar active nanocrystalline ferrite, MFe_2O_4 (M: Ca, Zn, Mg) photocatalyst by microwave irradiation. Solid State Commun. 151, 470–473.

30. J. Cao, T. Kako, P. Li, S. Ouyang, J. Ye (2011) Fabrication of p-type $CaFe_2O_4$ nanofilms for photoelectrochemical hydrogen generation. Electrochem. commun, 13, 275–278.

31. Z. Zhang, W. Wang (2014) Solution combustion synthesis of $CaFe_2O_4$ nanocrystal as a magnetically separable photocatalyst. Mater. Lett. 133, 212–215.

32. L. Khanna, N.K. Verma (2013) Synthesis, characterization and in vitro cytotoxicity study of calcium ferrite nanoparticles. Mater. Sci. Semicond. Process. 16, 1842–1848.

33. S. Verma, P.A. Joy, Y.B. Khollam, H. S. Potdar, S.B. Deshpande (2004) Synthesis of nanosized $MgFe_2O_4$ powders by microwave hydrothermal method Mater. Lett. 58, 1092–1095.

34. T. Sasaki, S. Ohara, T. Naka, J. Vejpravova, V. Sechovsky, M. Umetsu, S. Takami, B. Jeyadevan, T. Adschiri (2010) Continuous synthesis of fine $MgFe_2O_4$ nanoparticles by supercritical hydrothermal reaction. J. Supercrit. Fluids. 53, 92–94.

35. X. Chen, Y. Dai, W. Huang (2015) Novel $Ag_3PO_4/ZnFe_2O_4$ composite photocatalyst with enhanced visible light photocatalytic activity. Mater. Lett. 145, 125–128.

36. G. Zhao, L. Liu, J. Li, Q. Liu (2016) Efficient removal of dye MB: Through the combined action of adsorption and photodegradation from $NiFe_2O_4/Ag_3PO_4$. J. Alloys Compd. 664, 169-174.

37. B. Velaga, P. Shanbogh, D. Swain, Ch. Narayana, N. Sundaram (2018) High Surface Area SnO_2-Ta_2O_5 Composite for Visible Light Driven Photocatalytic Degradation of an Organic Dye, J. Photochem. Photobiol. https://doi.org/10.1111/php.12896.

38. D. Das, A. Samal, J. Das, A. Dash, H. Gupta (2014) One-Pot Fabrication of RGO–Ag_3VO_4 Nanocomposites by in situ Photoreduction using Different Sacrificial Agents: High Selectivity Toward Catechol Synthesis and Photodegradation Ability. J. Photochem. Photobiol. 90, 57–65.

39. H. Liu, Y. Wang, L. Shi, R. Xu, L. Huang, Sh. Tan (2016) Utilization of reduced graphene oxide for the enhancement of photocatalytic property of TiO_2 nanotube. Desalin water treat. 57, 13263–13272.

40. N. Zhang, Y. Zhang, Y. Xu (2012) Recent progress on graphene-based photocatalysts: current status and future perspectives. Nanoscale. 4, 5792–5813.

41. D. Lang, T. Shen, Q. Xiang (2015) Roles of MoS_2 and Graphene as Cocatalysts in the Enhanced Visible-Light Photocatalytic H_2 Production Activity of Multiarmed CdS Nanorods. ChemCatChem. 7, 943 – 951.

42. J. Theurich, M. Lindner, D.W. Bahnemann (1996)Photocatalytic Degradation of 4-Chlorophenol in Aerated Aqueous Titanium Dioxide Suspensions: A Kinetic and Mechanistic Study. Langmuir. 12, 6368–6376.

43. W.S. Hummers Jr, R. E. Offeman (1958) Preparation of graphitic oxide. J. Am. Chem. Soc. 80, 1339–1339.

44. E. Akbarzadeh, S. R. Setayesh and M. R. Gholami (2016) Synthesis of the visible-light-

driven $Ag_3VO_4/Ag_3PO_4/Ag$ photocatalysts with enhanced photocatalytic activity. RSC Adv. 18, 14909-14915.

45. Y. Shen, Y. Wu, X. Li, Q. Zhao,Y. Hou (2013) One-pot synthesis of $MgFe_2O_4$ nanospheres by solvothermal method. Mater. Lett. 96, 85–88.

46. G. Botelho, J. Andres, L. Gracia, L.S. Matos, E. Longo (2016) Photoluminescence and Photocatalytic Properties of Ag_3PO_4 Microcrystals: An Experimental and Theoretical Investigation. Chempluschem. 81, 202–212.

47. N. Aina, W. Shaheena, B. Bashira, N. Abdelsalamb, M. Warsia, M. Khanc, M. Shahid (2016) Electrical, magnetic and photoelectrochemical activity of $rGO/MgFe_2O_4$ nanocomposites under visible light irradiation. Ceramics International. 42, 12401-12408.

48. T.K. Pathak, N. H. Vasoya, V.K. Lakhani, K.B. Modi (2010) Structural and magnetic phase evolution study on needle-shaped nanoparticles of magnesium ferrite. Ceram. Int. 36, 275–281.

49. S. Zhang, J. Li, X. Wang, Y. Huang, M. Zeng and J. Xu (2014) In situ ion exchange synthesis of strongly coupled Ag@ $AgCl/g-C_3N_4$ porous nanosheets as plasmonic photocatalyst for h ighly efficient visible-light photocatalysis. Appl. Mater. Interfaces. 6, 22116-22125.

50. B. Jiang, Y. Wang, Jian-Q. Wang, Ch. Tian, W. Li, Q. Feng, Q. Pan, H. Fu (2013) In Situ Fabrication of Ag/Ag_3PO_4/Graphene Triple Heterostructure Visible-Light Photocatalyst through Graphene-Assisted Reduction Strategy. ChemCatChem. 5, 1359–1367.

51. M.Z. Naik, A.V. Salker (2016) Tailoring the super-paramagnetic nature of $MgFe_2O_4$ nanoparticles by In^{3+} incorporation. Mater. Sci. Eng B. 211, 37–44.

52. K. He, J. Xie, M. Li, X. Li (2018) In situ one-pot fabrication of $g-C_3N_4$ nanosheets/NiS cocatalyst heterojunction with intimate interfaces for efficient visible light photocatalytic H_2 generation. Appl. Surf. Sci. 430, 208-217.

53. N. Mohaghegh, E. Rahimi (2016) $BiPO_4$ photocatalyst employing synergistic action of Ag/Ag_3PO_4 nanostructure and graphene nanosheets. Solid. State. Sciences. 56, 10-15.

54. A. Kumar, A. Kumara, G. Sharma, M. Naushad, R. Cataluna Veses, A. Ghfar, F. Stadler, M. Rizwan Khan (2017) Solar-driven photodegradation of 17-β-estradiol and Ciprofloxacin from waste water and CO_2 conversion using sustainable Coal-char/polymeric-gC_3N_4/RGO metal free nano-hybrids. New J. Chem. 41**,** 10208-10224 .

55. H. Wang, L. Shen, F.Fu. Guo, Y. Liang (2016) Design and construction of the sandwich-like Z-scheme multicomponent CdS/Ag/Bi_2MoO_6 heterostructure with enhanced photocatalytic performance in RhB photodegradation. New J. Chem. 40, 8614-8624.

56. X. Yuan, H. Wang, Y. Wu, G. Zeng, X. Chen, L. Leng, Zh. Wu, H. Li (2016) One-pot selfassembly and photoreduction synthesis of silver nanoparticle-decorated reduced graphene oxide/MIL-125(Ti) photocatalyst with improved visible light photocatalytic activity. Appl. Organometal Chem. 30, 289–296.

57. Zh. Xue, T. Wang, B. Chen, T. Malkoske, Sh. Yu, Y. Tang (2015) Degradation of Tetracycline with $BiFeO_3$ Prepared by a Simple Hydrothermal Method. Materials. 8, 6360-6378.

58. F. Zhang, Sh. Zou, T. Wang, Y. Shi, P. Liu (2017) CeO_2/Bi_2WO_6 Heterostructured Microsphere with Excellent Visible-light-driven Photocatalytic Performance for Degradation of Tetracycline Hydrochloride. J. Photochem. Photobiol. 93, 1154-1164.

59. A. Chithambararaj, N.S. Sanjini, A.C. Bose, S, Velmathi (2013) Flower-like hierarchical h-MoO_3: new findings of efficient visible light driven nano photocatalyst for methylene blue degradation. Catal. Sci. Technol. 3, 1405-1414.

60. Ch. Zhang, Y. Zhou, J. Bao, Y. Zhang, Sh. Zhao, J. Fang, W. Chen, X. Sheng (2017) Hierarchical TiO_2 nanosheet-assembled nanotubes with dual electron sink functional sites for efficient photocatalytic degradation of rhodamine B. Appl Organometal Chem. 4204.

61. Q. Huang, M. Cao, Z. Ai, L. Zhang (2015) Reactive oxygen species dependent degradation pathway of 4-chlorophenol with Fe@Fe_2O_3 core-shell nanowires. Appl. Catal. B Environ. 162, 319–326.

62. C. Yang, Q. Li, L. Tang, K. Xin, A. Bai, Y. Yu (2015) Synthesis, photocatalytic activity, and photogenerated hydroxyl radicals of monodisperse colloidal ZnO nanospheres. Appl. Surf. Sci. 357, 1928-1938.

63. N. Kaur, S. Kaur Shahi, V. Singh (2016) Choline Chloride Assisted Synthesis of N and Metal Codoped TiO_2 and their Photocatalytic Activity under Visible Light. J. Photochem. Photobiol. 92, 69–75.

64. S. Sivakumar, A. Selvaraj, A. Kandasamy Ramasamy (2013) Photocatalytic Degradation of Organic Reactive Dyes over $MnTiO_3/TiO_2$ Heterojunction Composites Under UV-Visible Irradiation. J. Photochem. Photobiol. 89, 1047–1056.

Figure Captions:

Fig. 1. Spectrum distribution of the Visible light source provided by a 250-W mercury lamp with a UV cut off filter (visible light ≥420 nm).

Fig. 2. FT-IR spectra of (a) $CaFe_2O_4$, (b) Ag_3PO_4, (c) $CaFe_2O_4/Ag_3PO_4$(1:3), (d) rGO/$CaFe_2O_4/Ag_3PO_4$(1:3:9).

Fig. 3. XRD patterns of (a) Ag_3PO_4, (b) $CaFe_2O_4/Ag_3PO_4$; the iconograph in (b) is the XRD pattern of $CaFe_2O_4$ and (c) rGO/$CaFe_2O_4/Ag_3PO_4$.

Fig. 4. FESEM image of (a) neat $CaFe_2O_4$, (b) rGO/$CaFe_2O_4$, (c) Ag_3PO_4, (d) $CaFe_2O_4/Ag_3PO_4$ (1:3), (e, f) rGO/$CaFe_2O_4/Ag_3PO_4$ (1:3:9).

Fig. 5. Raman spectra of (a) $CaFe_2O_4$ nanoparticles and (b) rGO/$CaFe_2O_4$ nanocomposites.

Fig. 6. Magnetization curve of $CaFe_2O_4$, rGO/$CaFe_2O_4/Ag_3PO_4$ (1:3:9).

Fig. 7. The UV–Vis DRS and the band gap for (a) $CaFe_2O_4$, (b) Ag_3PO_4, (c) $CaFe_2O_4/Ag_3PO_4$(1:3), (d) rGO/$CaFe_2O_4/Ag_3PO_4$(1:3:9).

Fig. 8. EIS Nyquist plots of the Ag_3PO_4, rGO/$CaFe_2O_4/Ag_3PO_4$ (1:3:9), rGO/$MgFe_2O_4/Ag_3PO_4$ (1:3:9).

Fig. 9. The degradation efficiency for MB (25 mg/L) removal in the process of the $CaFe_2O_4$, $CaFe_2O_4/Ag_3PO_4$ and rGO/$CaFe_2O_4/Ag_3PO_4$ nanocomposites under visible light irradiation ([catalyst]= 2 g/L).

Fig. 10. The degradation efficiency for MO (25 mg/L) removal in the process of the $CaFe_2O_4$, $CaFe_2O_4/Ag_3PO_4$ and rGO/$CaFe_2O_4/Ag_3PO_4$ nanocomposites under visible light irradiation ([catalyst]= 2 g/L).

Fig. 11. The degradation efficiency for 4-CP (25 mg/L) removal in the process of the rGO/$CaFe_2O_4$/Ag_3PO_4 and rGO/$MgFe_2O_4$/Ag_3PO_4 nanocomposites under visible light irradiation ([catalyst]= 2 g/L).

Fig. 12. Linear-log plot for the photocatalytic degradation of MB in the presence of prepared samples under visible light irradiation.

Fig. 13. The degradation rate constant of the fabricated catalysts for the photocatalytic degradation of MB under visible light irradiation.

Fig. 14. The degradation efficiency for MB removal using different amount of rGO/$CaFe_2O_4$/Ag_3PO_4 (1:3:9) and different concentration of initial dye under visible light irradiation.

Fig. 15. Effect of different scavengers on degradation of MB by rGO/$CaFe_2O_4$/Ag_3PO_4 under the optimized conditions.

Fig. 16. (a) MB, (b) MO, (c) 4-CP degradation performance in consecutive cycles using the recycled rGO/$CaFe_2O_4$/Ag_3PO_4 (1:3:9) photocatalyst through magnetic separation.

Fig. 17. Schematic illustration of the proposed reaction mechanism for the photocatalytic degradation of the dyes in the presence of rGO/$CaFe_2O_4$(M=Ca, Mg)/Ag_3PO_4 nanocomposite.

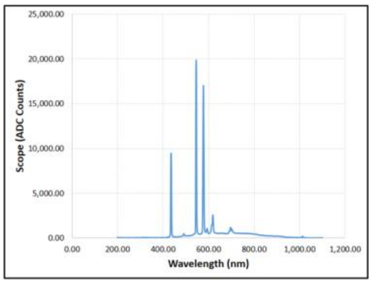
25,000.00
20,000.00
15,000.00
10,000.00
5,000.00
0.00
Scope (ADC Counts)
0.00
200.00
400.00
600.00
800.00
1,000.00
1,200.00
Wavelength (nm)

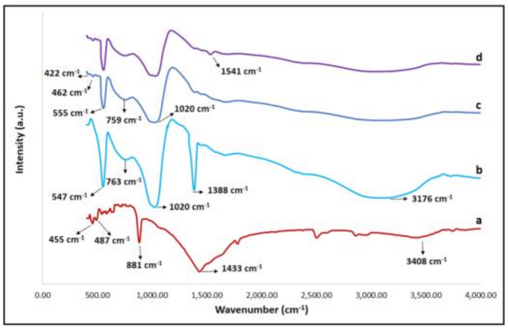
d
1541 cm⁻¹
422 cm⁻¹
462 cm⁻¹
555 cm⁻¹
759 cm⁻¹
1020 cm⁻¹
c
b
763 cm⁻¹
547 cm⁻¹
1020 cm⁻¹
1388 cm⁻¹
3176 cm⁻¹
a
455 cm⁻¹
487 cm⁻¹
881 cm⁻¹
1433 cm⁻¹
3408 cm⁻¹
Intensity (a.u.)
0.00
500.00
1,000.00
1,500.00
2,000.00
2,500.00
3,000.00
3,500.00
4,000.00
Wavenumber (cm⁻¹)

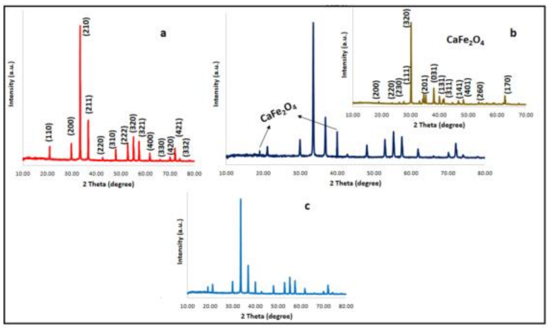
a
Intensity (a.u.)
(110)
(200)
(210)
(211)
(220)
(310)
(222)
(320)
(321)
(400)
(330)
(420)
(421)
(332)
10.00
20.00
30.00
40.00
50.00
60.00
70.00
80.00
2 Theta (degree)
b
Intensity (a.u.)
CaFe2O4
10.00
20.00
30.00
40.00
50.00
60.00
70.00
80.00
2 Theta (degree)
CaFe2O4
(200)
(220)
(230)
(111)
(320)
(201)
(031)
(131)
(311)
(141)
(401)
(260)
(170)
10.00
20.00
30.00
40.00
50.00
60.00
70.00
2 Theta (degree)
c
Intensity (a.u.)
10.00
20.00
30.00
40.00
50.00
60.00
70.00
80.00
2 Theta (degree)

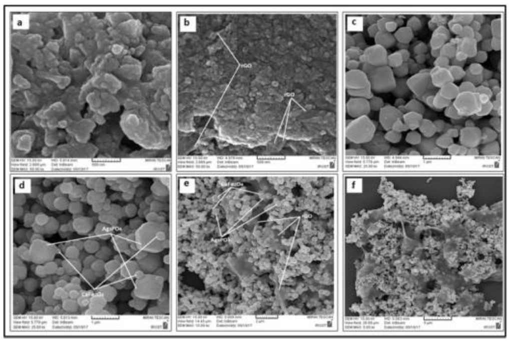
a
b
rGO
rGO
c
d
Ag3PO4
CaFe2O4
e
CaFe2O4
rGO
Ag3PO4
f
500 nm
500 nm
1 µm
1 µm
2 µm
5 µm

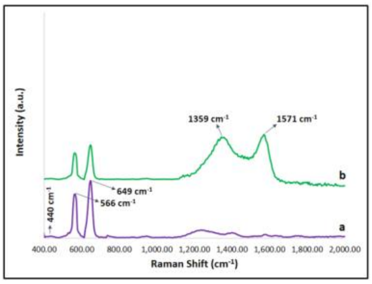
Intensity (a.u.)
1359 cm-1
1571 cm-1
b
649 cm-1
566 cm-1
440 cm-1
a
400.00
600.00
800.00
1,000.00
1,200.00
1,400.00
1,600.00
1,800.00
2,000.00
Raman Shift (cm-1)

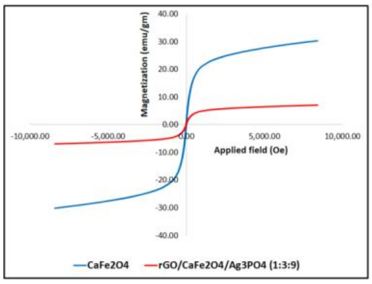
Magnetization (emu/gm)
40.00
30.00
20.00
10.00
0.00
-10.00
-20.00
-30.00
-40.00
-10,000.00
-5,000.00
0.00
5,000.00
10,000.00
Applied field (Oe)
CaFe2O4
rGO/CaFe2O4/Ag3PO4 (1:3:9)

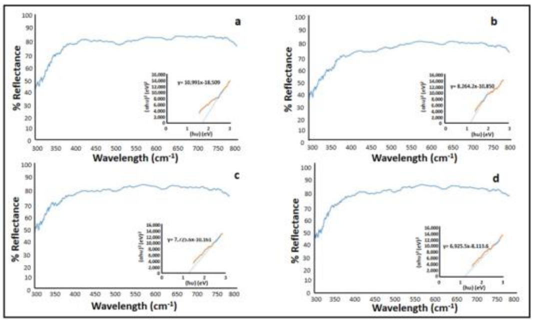
a
b
c
d
% Reflectance
Wavelength (cm⁻¹)
100
90
80
70
60
50
40
30
20
10
0
300
350
400
450
500
550
600
650
700
750
800
(αhυ)² (eV)²
(hυ) (eV)
0
1
2
3
16,000
14,000
12,000
10,000
8,000
6,000
4,000
2,000
y= 10,991x-18,509
y= 8,264.2x-10,850
y= 6,925.5x-8,113.6

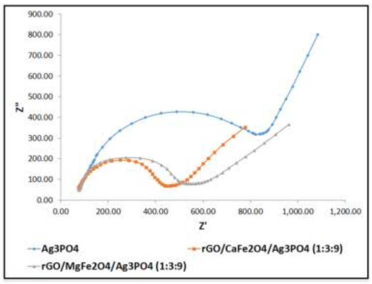
Z"
Z'
900.00
800.00
700.00
600.00
500.00
400.00
300.00
200.00
100.00
0.00
0.00
200.00
400.00
600.00
800.00
1,000.00
1,200.00
Ag3PO4
rGO/CaFe2O4/Ag3PO4 (1:3:9)
rGO/MgFe2O4/Ag3PO4 (1:3:9)

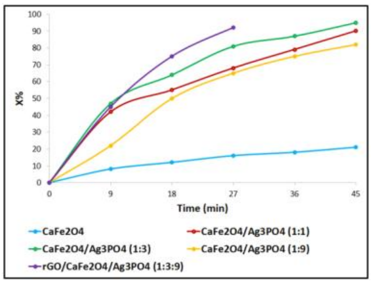
X%
Time (min)
100
90
80
70
60
50
40
30
20
10
0
0
9
18
27
36
45
CaFe2O4
CaFe2O4/Ag3PO4 (1:1)
CaFe2O4/Ag3PO4 (1:3)
CaFe2O4/Ag3PO4 (1:9)
rGO/CaFe2O4/Ag3PO4 (1:3:9)

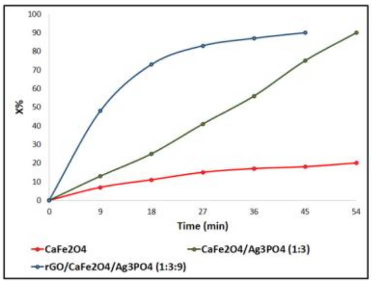
100
90
80
70
60
50
40
30
20
10
0
X%
0
9
18
27
36
45
54
Time (min)
CaFe2O4
CaFe2O4/Ag3PO4 (1:3)
rGO/CaFe2O4/Ag3PO4 (1:3:9)

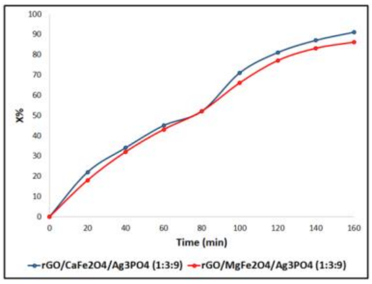
100
90
80
70
60
50
40
30
20
10
0
X%
0
20
40
60
80
100
120
140
160
Time (min)
rGO/CaFe2O4/Ag3PO4 (1:3:9)
rGO/MgFe2O4/Ag3PO4 (1:3:9)

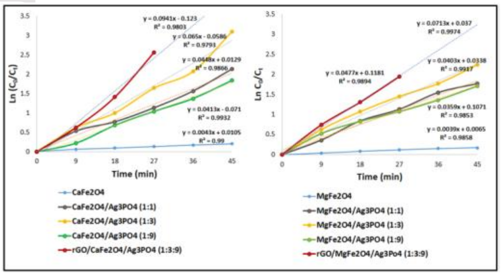
3.5
3
2.5
2
1.5
1
0.5
0
Ln (C0/Ct)
y = 0.0941x - 0.123
R² = 0.9803
y = 0.065x - 0.0586
R² = 0.9793
y = 0.0448x + 0.0129
R² = 0.9866
y = 0.0413x - 0.071
R² = 0.9932
y = 0.0043x + 0.0105
R² = 0.99
0
9
18
27
36
45
Time (min)
CaFe2O4
CaFe2O4/Ag3PO4 (1:1)
CaFe2O4/Ag3PO4 (1:3)
CaFe2O4/Ag3PO4 (1:9)
rGO/CaFe2O4/Ag3PO4 (1:3:9)
3.5
3
2.5
2
1.5
1
0.5
0
Ln C0/Ct
y = 0.0713x + 0.037
R² = 0.9974
y = 0.0477x + 0.1181
R² = 0.9894
y = 0.0403x + 0.0338
R² = 0.9917
y = 0.0359x + 0.1071
R² = 0.9853
y = 0.0039x + 0.0065
R² = 0.9858
0
9
18
27
36
45
Time (min)
MgFe2O4
MgFe2O4/Ag3PO4 (1:1)
MgFe2O4/Ag3PO4 (1:3)
MgFe2O4/Ag3PO4 (1:9)
rGO/MgFe2O4/Ag3Po4 (1:3:9)

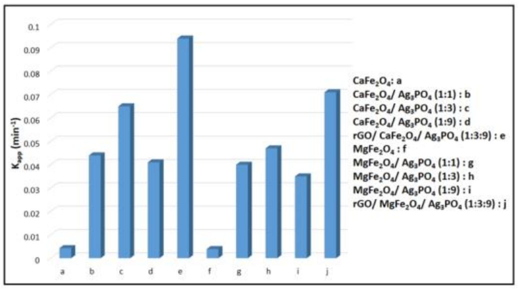
0.1
0.09
0.08
0.07
0.06
0.05
0.04
0.03
0.02
0.01
0
K_{app} (min^{-1})
a
b
c
d
e
f
g
h
i
j
$CaFe_2O_4$: a
$CaFe_2O_4$/ Ag_3PO_4 (1:1) : b
$CaFe_2O_4$/ Ag_3PO_4 (1:3) : c
$CaFe_2O_4$/ Ag_3PO_4 (1:9) : d
rGO/ $CaFe_2O_4$/ Ag_3PO_4 (1:3:9) : e
$MgFe_2O_4$: f
$MgFe_2O_4$/ Ag_3PO_4 (1:1) : g
$MgFe_2O_4$/ Ag_3PO_4 (1:3) : h
$MgFe_2O_4$/ Ag_3PO_4 (1:9) : i
rGO/ $MgFe_2O_4$/ Ag_3PO_4 (1:3:9) : j

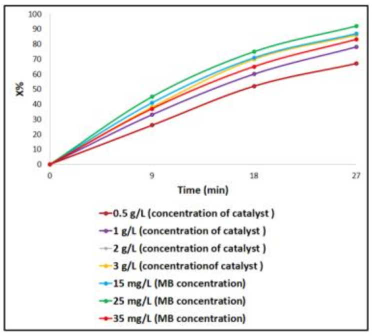
100
90
80
70
60
50
40
30
20
10
0
X%
0
9
18
27
Time (min)
0.5 g/L (concentration of catalyst)
1 g/L (concentration of catalyst)
2 g/L (concentration of catalyst)
3 g/L (concentrationof catalyst)
15 mg/L (MB concentration)
25 mg/L (MB concentration)
35 mg/L (MB concentration)

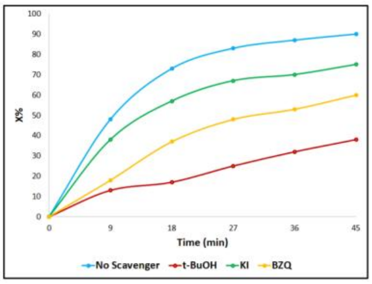
100
90
80
70
60
50
40
30
20
10
0
X%
0
9
18
27
36
45
Time (min)
No Scavenger
t-BuOH
KI
BZQ

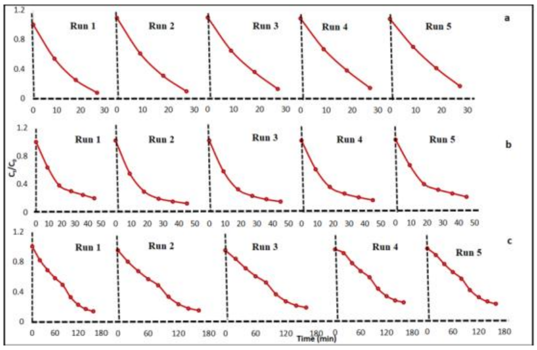
a
b
c
Run 1
Run 2
Run 3
Run 4
Run 5
C_t/C_0
0
0.4
0.8
1.2
0 10 20 30
0 10 20 30 40 50
0 60 120 180
Time (min)

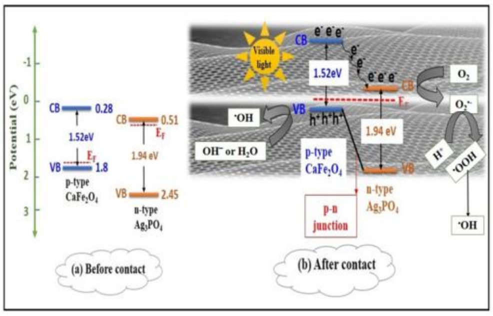
Potential (eV)
-1
0
1
2
3
CB 0.28
1.52eV
E_F
VB 1.8
p-type $CaFe_2O_4$
CB 0.51
E_F
1.94 eV
VB 2.45
n-type Ag_3PO_4
(a) Before contact
Visible light
CB
$e^- e^- e^-$
1.52eV
$e^- e^- e^-$
CB
E_F
O_2
$O_2^{\bullet -}$
VB
$h^+h^+h^+$
$^\bullet OH$
OH^- or H_2O
p-type $CaFe_2O_4$
1.94 eV
VB
H^+
$^\bullet OOH$
n-type Ag_3PO_4
p-n junction
$^\bullet OH$
(b) After contact

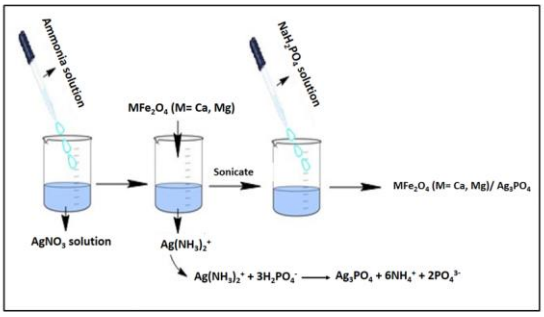
Ammonia solution
MFe$_2$O$_4$ (M= Ca, Mg)
NaH$_2$PO$_4$ solution
Sonicate
MFe$_2$O$_4$ (M= Ca, Mg)/ Ag$_3$PO$_4$
AgNO$_3$ solution
Ag(NH$_3$)$_2^+$
Ag(NH$_3$)$_2^+$ + 3H$_2$PO$_4^-$ ⟶ Ag$_3$PO$_4$ + 6NH$_4^+$ + 2PO$_4^{3-}$

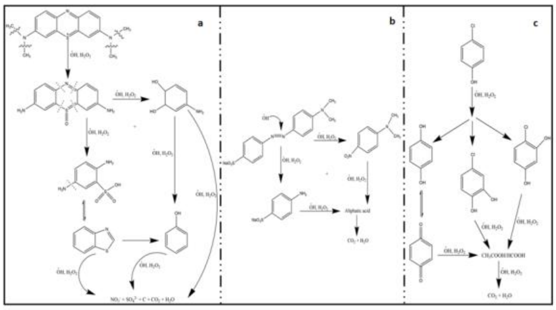
a
b
c
ȮH, H$_2$O$_2$
Aliphatic acid
CO$_2$ + H$_2$O
CH$_3$COOHHCOOH
NO$_3^-$ + SO$_4^{2-}$ + C + CO$_2$ + H$_2$O